Intravital imaging of osteocyte $\alpha_v\beta_3$ integrin dynamics with locally injectable fluorescent nanoparticles

Melia Matthews[1,], Emily Cook[1,], Nada Naguib[1,], Uli Wiesner[2,], and Karl Lewis[1,✉]

[1]Department of Biomedical Engineering, Cornell University, 237 Tower Rd, Ithaca,14850, New York, USA
[2]Department of of Materials Science and Engineering, Cornell University, Bard Hall 210, Ithaca, 14850, New York, USA

Abstract

Osteocytes are the resident mechanosensory cells in bone. Bone mechanotransduction is necessary for skeletal homeostasis and adaptation to its mechanical environment. Integrin proteins have been proven to play an integral role in osteocyte mechanotransduction, however the mechanisms of their role is not well stratified *in vivo*. Intravital imaging with multiphoton microscopy presents an opportunity to study molecular level mechanobiological events *in vivo*, and could be used to study integrin dynamics. However, limitations exist with respect to fluorescent intravital probes because of the optical scattering and low signal to noise ratio caused by the mineralized bone matrix. Here we demonstrate that ultrasmall and bright surface functionalized fluorescent core-shell silica nanoparticles synthesized in water (<7nm diameter), known as Cornell Prime Dots (C'Dots), are well-suited to overcome bone's imaging impediments. We report validation studies for C'Dots as novel, locally injected *in vivo* osteocyte imaging tools for both general use and for targeting $\alpha_v\beta_3$ integrin. C'Dots are shown to be successful as a targeted, locally administered fluorescent probe for intravital bone imaging. The pharmacokinetics of C'Dots reveal distinct sex differences in nanoparticle cycling and clearance in osteocytes, which may represent a novel topic of study in bone biology. Integrin-targeted C'Dots were investigated for their potential to study osteocyte integrin dynamics. To the best of our knowledge, we show the first evidence of osteocyte integrin endocytosis and recycling *in vivo*. Our results suggest that ultrasmall and bright nanoparticles, like C'Dots, represent powerful new probes for intravital osteocyte imaging, with targeting potential for observing bone mechanobiological mechanisms *in vivo*.

osteocyte | fluorescent probe | integrin | multiphoton microscopy
Correspondence: *kjl235@cornell.edu*

Introduction

Osteocytes are embedded in the mineralized matrix of bone and represent 90-95% of all cells found in bone tissue (1). Previously thought to be quiescent place-holders, it is now understood that they act as master conductors and regulators of skeletal health and homeostasis (2, 3). For their most important role, osteocytes are the resident mechanosensors in bone, incorporating mechanical signals along their processes and relaying biochemical signals through a highly interconnected dendritic network to matrix producing osteoblast cells and bone resorbing osteoclast cells in response to their mechanical environment (4–6).

Generally, cell biology investigation in bone has used a combination of cell culture and high resolution imaging of thin tissue sections. *In vitro* work studying osteocyte mechanobiology over the last 25 years has established many details about osteocyte anatomy and mechanotransduction via these methods. For example, McNamara and colleagues used electron microscopy to show physical evidence of the point attachments between osteocyte processes and their surrounding matrix (7), informing the updated model for mechanotransduction put forth by Qin et al.(8). Osteocyte-like cell lines *in vitro* exhibit fluid flow induced activation leading to calcium signaling (5) and bone anabolic cytokine expression (9). Mechanical stimulation by strain induced fluid flow is sensed by osteocytes and the signal is transduced throughout their cellular network, stimulating mineral deposition and resorption in response to the mechanical environment (10). Additionally, it has been shown that osteocytes sense mechanical stimulation through a number of transmembrane proteins and channels along dendrites within the bone lacunar-canalicular space (LCS) (7). Integrin proteins are among those implicated as being key means of mechanical activation in osteocyte mechanotransduction (11, 12).

Integrins are heterodimeric proteins found within the mechanosomes of osteocytes (11), and integrin mediated strain amplification has been shown to be a key functional mechanism for cell activation to physiological fluid flow conditions (7, 13). Integrins are dynamic proteins involved in cell adhesion and mobility, and undergo endocytosis and recycling in numerous cell types (14–16). A sepcific integrin subclass, $\alpha_v\beta_3$ integrins, undergo endocytosis as part of their role in cell mgration and focal adhesion (17–19), and are heavily expressed on osteocyte processes (13). The dynamics of integrin proteins have been shown to involve clatherin-mediated cycling in osteoblast-like cells *in vitro* (20), but have not been previously observed in osteocytes.

While the above *in vitro* and *ex vivo* studies provided new information on the environment of osteocytes, these type of studies also lose vital connections to the 3D microenvironment, which are crucial for the mechanisms of osteocyte mechanotransduction (21, 22). Recent advancements in imaging have made it possible to study osteocytes *in vivo*, providing an opportunity to expand our understanding of

known osteocyte mechanotransduction mechanisms and discover new details about their behavior in physiologically intact conditions.

Intravital imaging with multiphoton microscopy (MPM) represents a powerful tool to study osteocyte mechanobiology. Simultaneous absorption of multiple low energy photons at the focal point of the laser beam results in distinct imaging advantages, including reduced off-target excitation and a drastically lower signal to noise ratio. This has allowed for osteocytes and other bone cells to be visualized *in vivo* with genetically encoded fluorescent probes (23). However, the dense optical scattering nature of mineralized bone matrix has limited research questions to bulk cytosolic events such as calcium signaling (24). While useful for understanding cell and tissue level properties, research into subcellular or molecular events *in vivo* has been restricted. There are very few exogenous probes that have been developed to target the subcellular dynamics of cells within bone, especially osteocytes (25, 26). A solution to this imaging impediment is ultrasmall surface functionalized fluorescent core-shell silica nanoparticles known as Cornell Prime Dots (C'Dots), which have originally been developed for various bioimaging applications, both *in vitro* and *in vivo* (27–29).

C'Dots are bright nanoparticles whose ultrasmall size (hydrodynamic diameter <7nm) permits access through the LCS to the area surrounding osteocyte cells (30). Their ultrasmall size leads to favorable biodistribution and pharmacokinetics profiles, proven in multiple human clinical trials and establishing their safe use (31, 32). Their silica core increases the brightness of the encapsulated dyes (e.g., cyanine dyes like Cy5) via a combination of increases in radiative rates and decreases in non-radiative rates (27, 33–35). An additional beneficial aspect of C'Dots is that their brush-like poly(ethylene glycol) (PEG) shell (36), which minimizes protein corona formation and also enables facile covalent surface functionalization with various ligands, e.g., targeting or drug moieties, transforming them into targeted imaging or therapeutic probes (37–40). Here we validate the use of C'Dots as an imaging tool for osteocytes *in vivo*. Following the initial C'Dot validation, we use functionalized C'Dots with a RGD motif that targets $\alpha_v\beta_3$ integrins (41, 42), which are highly expressed on the cell processes of osteocytes (7). These RGD bearing C'Dots provide the first opportunity to interrogate integrin activity/dynamics in osteocytes *in vivo*, with 3D microarchitecture, fluid environment, and endocrine interactions in place. We use a local, subcutaneous injection of control and RGD C'Dots as novel *in vivo* osteocyte and integrin dynamics imaging tools and test the hypothesis that RGD functionalization increases the lifespan of C'Dots in osteocytes *in vivo*.

Methods

Animals: Male and female 16-20 week old C57Bl/6J mice (Jackson Laboratory, Bar Harbor, ME) were used in these experiments. All procedures were approved by the Institutional Animal Care and Use Committees at Cornell University.

Synthesis of PEGylated and cRGDyC Silica Core-Shell Nanoparticles: Plain (PEG-C'Dots) and targeted (cRGDyC-C'Dots, labeled RGD-C'Dots in the rest of this manuscript) ultrasmall fluorescent core-shell silica nanoparticles (C'Dots) were synthesized by a modified Stöber process in water as previously described (27, 42). This synthesis approach involves the addition of tetramethyl orthosilicate (TMOS) (Sigma Aldrich) and silane-functionalized Cy5 organic dye (Lumiprobe) into a solution of water and ammonium hydroxide at a pH of 8 (27). The reaction was conducted at room temperature under vigorous stirring for 24 hours and was terminated by the addition of PEG-silane (EO6-9) (Gelest Inc). In the case of the cRGDyC C'Dots, cRGDy peptides (BioSynth Ltd.) containing the sequence cyclo-(Arg-Gly-Asp-Tyr) were conjugated to a heterobifunctional PEG-silane with a maleimido group through cysteine-maleimide linkage (Santa Cruz Biotechnology). This cRGDyC-PEG-silane was then added during the PEGylation step along with the unmodified PEG-silane (Gelest). Particles were then purified through gel permeation chromatography (GPC, BioRad Laboratories) prior to further optical characterization. Absorption and emission spectral profiles of the particles were obtained using a Varian Cary 5000 spectrophotometer (Varian, Palo Alto, CA) and a fluorescence spectrofluorometer (Photon Technology International). The hydrodynamic radius, particle brightness and sample concentrations were determined using a homebuilt fluorescence correlation spectroscopy (FCS) set-up using a 633 nm excitation solid state laser (27). As described in the Supporting Information, the PEG-C'Dots and cRGDyC-C'Dots exhibited similar properties including hydrodynamic radii (5.6 nm and 5.3 nm, respectively) and number of dyes per particle (2.0 and 2.1, respectively) as derived from a combination of FCS and UV-VIS data sets using methods detailed elsewhere (38). The number of cRGDyC peptides per C'Dot was estimated to be 20 ligands.

Injection and Incubation: 15µL of C'Dots were administered into the hind paw of an isoflurane anesthetized mouse via a subcutaneous injection over the third metatarsal (MT3). The concentration of the injection was varied between 30µM and 10nM. Incubation time after injection was varied as well, from 5 minutes up to 24 hours. Mice were allowed normal cage activity during their incubation time, with an exception for the 5 minute timepoint.

Metatarsal Isolation Surgery: A shallow vertical incision was made between the second and third metatarsal of the mouse hind paw and overlying tendons were removed. The MT3 was functionally isolated from the rest of the paw with a stainless steel pin beneath the middiaphysis of the bone. The bone was then stabilized in a 3 point bending configuration and submerged in room temperature DPBS prior to imaging, as reported perviously (24).

C'Dot Imaging: Cy5 C'Dot (osteocyte) fluorescent signal inside the MT3 was visualized with multiphoton microscopy (MPM) (Bergamo II, Thorlabs). A 20x immersion objective (XLUMPLFLN, Olympus), 1090nm wavelength excitation, and a >647nm longpass filter acquisition was used for imag-

ing for C'Dots. A 35μM z-stack was taken for each mouse, starting 20μM beneath the bone surface, with 0.3μM steps between each frame and frame averaging of 7 frames per layer. For the Clearance Rate study, z-stacks were taken every 15 minutes for 3 hours after the initial 1 hour incubation.

C'Dot Image Analysis: Z-stacks were analyzed in ImageJ (U.S. National Institutes of Health, Bethesda, MD, https://imagej.nih.gv/ij). A macro was created to interpolate the regions of interest across all layers of the z-stack as well as filtering with despeckling and a Gaussian blur. Then 3D segmentation was run, creating objects for all cell volumes over a threshold intensity. The lower bound for threshold intensity was created as 3x SD between background fluorescence of different experimental groups. These objects were filtered by surface area (>1000 pixels) to ensure only real cell volumes were counted, and then mean intensity for each object was quantified using the 3D manager tool.

Calcein-AM Imaging and Co-localization: Calcein AM live cell stain (C-AM) was used for evaluating intracellular localization of C'Dots and was imaged at 920nm excitation and with a 490-560nm bandpass filter. To assess fluorescent signal overlap, z-stacks were taken of the same region of interest on the bone at both C'Dot and C-AM excitation/filtering. Both stacks were loaded into ImageJ for analysis. For C'Dot/C-AM co-localization analysis, individual cells labeled with C'Dots or C-AM were identified by eye and given their own ROI. Z-axis profiles of intensities were plotted and the range where signal increased from baseline into a spike was set as the bound of the signal.

Statistical Analyses: Differences between concentration groups and incubation time groups were assessed using a 2-way ANOVA followed by Tukey's multiple comparisons test. Clearance study analysis was done using a t test and 2-way ANOVAs. Analyses were performed in GraphPad Prism version 9.0 for Mac OS X (GraphPad Software, San Diego, CA, www.graphpad.com).

Results

Local Acute Delivery of C'Dots to Osteocytes *in vivo*. For the initial pilot experiments, PEGylated Cornell prime dots (PEG-C'dots) covalently encapsulating Cy5 fluorescent dye were locally injected subcutaneously into the hind paw of C57Bl/6J mice to assess their potential as an *in vivo* fluorescent marker for osteocytes. Using MPM excitation at 1090nm, i.e., in the near-infrared region (NIR), both collagen autofluorescence and C'Dot fluorescence were visualized in the MT3 diaphysis *in vivo* (**Figure 1**). C'Dot fluorescence was spatially diffuse through LCS in cortical bone, indicating that C'Dots are able to travel through the pores in the LCS and interact with osteocytes. To assess uptake of the C'Dots into living osteocytes, Calcein-AM (a live cell stain) was co-injected with C'Dots and imaged. Co-localization of C'Dots with Calcein-AM was observed and almost 70% of C'Dot cell signal was fully contained within the C-AM signal (**Figure 2**).

Non-Functionalized (Control) PEG-C'Dot Validation Experiments. After having success visualizing osteocytes with C'Dots, validation and optimization of their use as a novel osteocyte probe in mouse metatarsal bone *in vivo* was performed. A concentration dose-response curve and incubation time experiments were done. The concentration of C'Dot injections were varied from 30μM down to 10nM, incorporating the range of C'Dot concentrations previously used in the literature for soft tissue imaging and adding higher concentrations to account for the dense, scattering material of bone (41). Strong signal was seen down to 5μM, and became close to background fluorescence at 1μM and below (**Figure 3**). Reduction in signal with decreased C'Dot concentration was observed, as expected, and there were no significant differences between male and females at each concentration (**Figure 4A**). 10μM was found to represent the best working concentration for C'Dots because there is strong signal but it is not fully saturated. This will allow subtle variations in fluorescence to be observed and quantified. Then, holding the concentration steady, incubation time was varied from 5 minutes out to 24 hours, with seven distinct timepoints (5min, 30min, 1, 2, 4, 12, and 24hrs). Using described methods, fluorescence signal was quantifiable out to the 4hr incubation for both male and female groups (**Figure 4B**). Beyond those timepoints, the signal was too diffuse to be counted by 3D segmentation and filtering. Distinct biphasic trends in fluorescence intensity were observed between male and female mice. This result suggests unique dynamics in male and female bone tissue for the metabolism and clearance of C'Dots. Additionally, the 1hr timepoint had a consistent high intensity across the experimental groups, which will inform future experiments (**Figure 4C**).

RGD Functionalized C'Dot Validation Experiments. Once proof of concept for PEG-C'Dot use as an osteocyte probe was established and optimized concentration and incubation time were identified, a targeted C'Dot was tested to see if the fluorescence intensity or dynamics would change. C'Dots functionalized with RGD motifs that bind to $\alpha_v\beta_3$ integrins commonly expressed on osteocyte processes were obtained and tested using the same methodology as the non-functionalised C'Dots (**Figure 1C**). It was hypothesized that this integrin binding would allow C'Dot signal to be retained in the LCS/osteocyte for longer compared to non-targeted control PEG-C'Dots due to the assumption that integrins are not normally cleared from through the LCS under any known mechanisms. Concentration dose-response curve and incubation time were again assessed using the same groupings as the control PEG-C'Dot studies (**Figure 5A,B**). Signal was retained at slightly lower concentrations for RGD C'Dots compared to control PEG-C'Dots, above background fluorescence out to 100nM instead of 1μM. 10μM continued to be the preferred sub-saturation concentration. In terms of incubation time, signal was once again lost beyond 4hrs, confirming fast nanoparticle clearance. 1hr incubation retained

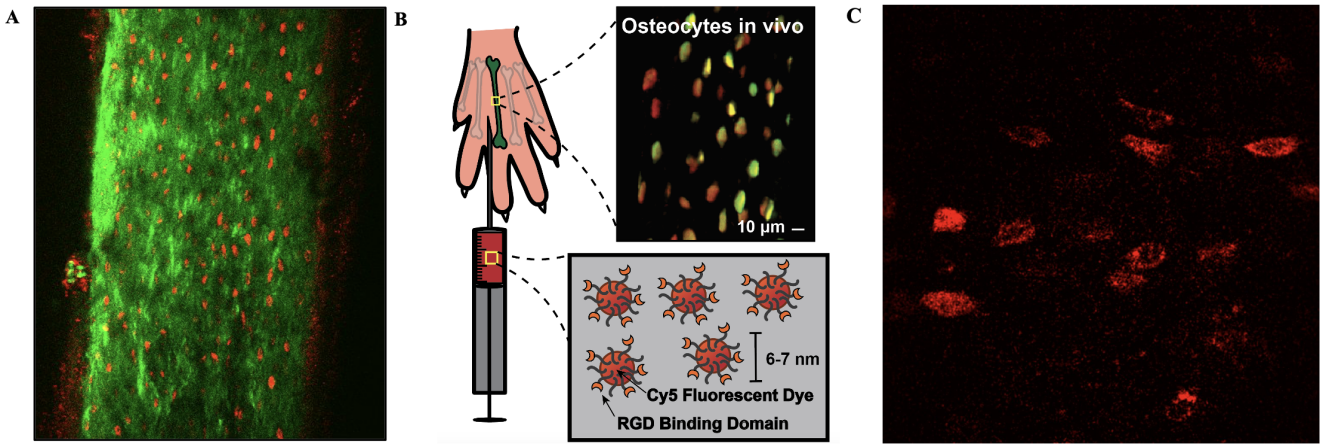

Fig. 1. C'Dots allow successful intravital imaging of osteocytes in mice after a local injection above the MT3 bone. A) Representative MT3 bone image with MPM excitation at 1090nm. Green is autofluorescence of bone collagen and red is Cy5 dye within C'Dots. B) Localization of C'Dots within osteocytes. Dual injection of live cell marker Calcein-AM (green) and C'Dots (Red), with overlap shown in yellow. Calcein AM was excited at 920nm and a 35µM z-stack was taken. The same z-stack was imaged again at 1090nm for the C'Dot signal. Channels were merged in ImageJ and image was taken in 3D project mode. Signal acquisition for C'Dot fluorescence used a >647nm longpass filter, and Calcein AM was visualized using a 490-560nm bandpass filter. C) RDG-C'Dots visualized at 80x zoom reveal subcellular localization of C'Dots within osteocytes (15µL injection, 10µM concentration).

high intensity signal across groups (**Figure 5C**). However, the biphasic intensity trend with incubation time seemed to be switched between males and females when using the RGD-C'Dots. Specifically, the strong drop in signal at the 30min incubation timepoint and subsequent rebound at the 1hr timepoint seen in control PEG-C'Dot females was now being seen in the RGD-C'Dot males. This suggests potential differences in integrin and C'Dot endocytosis and recycling depending on sex and C'Dot functionalization.

Clearance Rate of Functionalized RGD-C'Dots and Non-Functionalized PEG-C'Dots from LCS Over Time. After establishing concentration and incubation time in control PEG-C'Dots and targeted RGD-C'Dots, the dynamics of both groups of C'Dots were studied within the LCS over time in individual mice. This was done to better understand the pharmacokinetics of the C'Dots and to set a baseline measurement for serial PEG-C'Dot and RGD-C'Dot imaging. 10µM concentration and 1hr incubation time post injection were used, then a z-stack of a region of interest (ROI) on the MT3 was taken every 15min for up to 3hrs to see how the fluorescence of the C'Dots changed. The fluorescent signal of the 3D cell volumes was quantified using FIJI. The number of cells that were quantified decreased markedly over time and cleared in a distinct way between the sexes. Male mice, using either targeted RGD-C'Dots or control PEG-C'Dots, had total loss of 3D object signal after 1hr of imaging (as quantified by our methods). Female mice, on the other hand, retained at least some 3D object signal to the end of the experiment, displaying an unmistakable difference in trend line (**Figure 6A**). Male mice cleared the C'Dots from the LCS more quickly than their female counterparts, suggesting sexual dimorphism in terms of fluid flow and/or osteocyte C'Dot metabolism. This was confirmed by the fluorescent intensity of the 3D objects as well. Male cell volumes had lower average volumetric intensity compared to female mice (**Figure 6B,C**). However, an aspect not seen with the cell count results is that the targeted RGD-C'Dots and control PEG-C'Dots also have unique trends. Female cell volumes marked by RGD-C'Dots had a significantly lower intensity from control at the 30min timepoint, and retained that lower intensity over the remaining time of the experiment. Finally, male control PEG-C'Dot clearance occurred 30 minutes sooner compared to RGD-C'Dot clearance (**Figure 6C**). The trends in the quantified cell volume intensity data can be observed visually as well. C'Dot clearance from the LCS over time was visualized using a side-by-side video format comparing males to females (Supplementary Video 1, 2). For both control PEG-C'Dots and targeted RGD-C'Dots, it is clear that male mice lost signal much earlier compared to time-matched females.

Discussion

Osteocytes were successfully observed *in vivo* using MPM and C'Dots, locally injected, exogenous fluorescent probes. Our experiments establish the use of C'Dots as an osteocyte marker *in vivo*. These C'Dots provide a novel opportunity to interrogate osteocytes *in vivo*, with implication for anatomical and functional study applications. The current paucity of bone cell-specific exogenous fluorescent probes and the time and monetary expense of genetically modified fluorescent mouse lines make C'Dots a useful improvement in the realm of intravital bone cell imaging (23).

The co-localization data with Calcein AM (**Figure 2**) suggests that C'Dots are being absorbed into osteocytes, likely via endocytosis. This finding is supported by the fluorescent dynamics of both control PEG and RGD-C'Dots, which suggest that endocytosis results in clearance or degradation of the C'Dots over time. C'Dots have been shown to undergo endocytosis in other cell and tissue types, but their half-life in osteocytes and the LCS is remarkably short. Benezra et al. observed that C'Dot signal was retained in tissue for

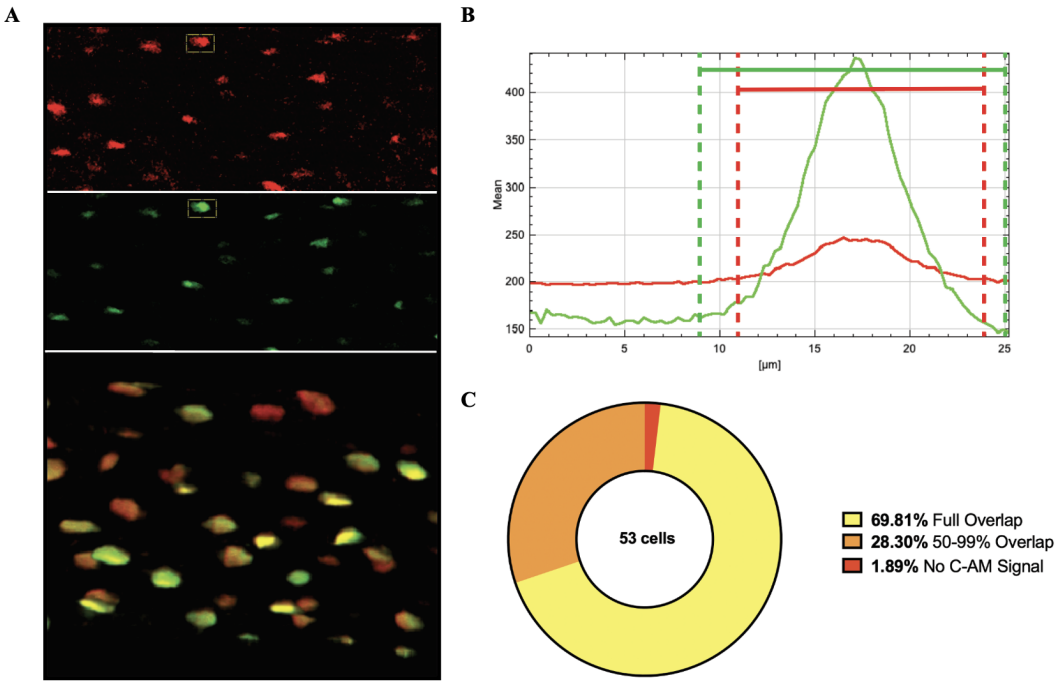

Fig. 2. C'Dot co-localization with Calcein-AM. A) Representative image of C-AM signal (green) and C'Dot signal (red) with example cell region of interest. 3D image overlay on the bottom. Channels were separated in ImageJ and individual cell ROIs were selected by eye. B) Example z-stack intensity profile plot of single ROI in both channels. The range of cell signal was established as increase from baseline signal. C) Quantified C'Dot and C-AM overlap. 53 cell ROIs were quantified. Nearly 70% of C'Dot signal was fully contained within the range of C-AM signal. Only one ROI with C'Dot signal did not have C-AM signal as well. All ROIs with C'AM signal had over 50% overlap with the C'Dot signal. Average overlap was 94.8%, SD = ±8.9%.

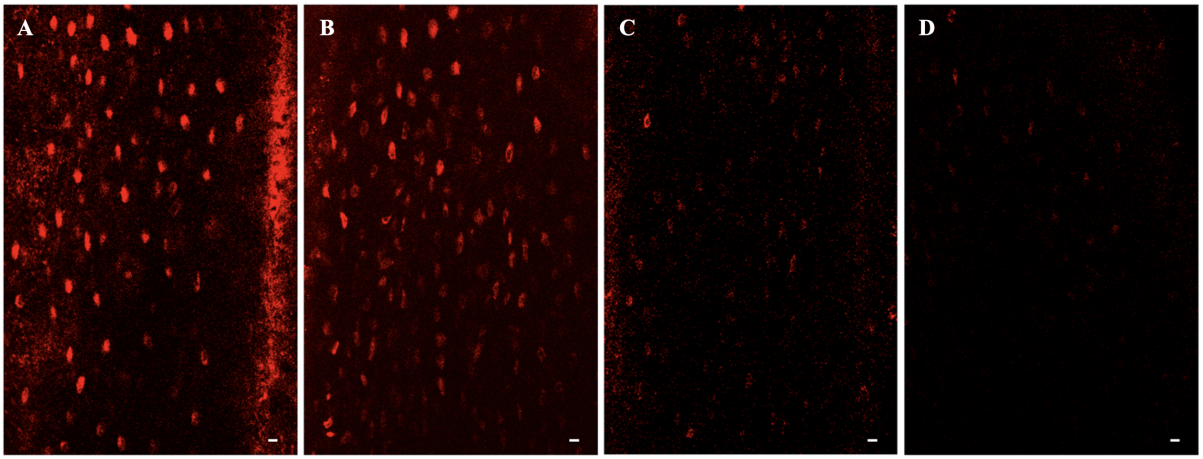

Fig. 3. C'Dot fluorescence intensity decreases with subcutaneous injection concentration. Representative static images of MT3 diaphysis osteocytes after 1 hour of incubation using injection concentrations of A) 30µM, B) 10µM, C) 5µM, D) 1µM in male mice. C'Dots were excited at 1090nm and emission was acquired with a >647nm longpass filter. Scale bar = 10µM.

multiple days (43), while signal from osteocytes within the LCS strongly dissipated only hours after injection. That the C'Dots clear from osteocytes much faster than other cell and tissue types is intriguing. Fast signal dissipation implies rapid trafficking of C'Dots. This type of trafficking is likely due to endocytosis of C'Dots followed by intracellular degradation or recycling to the cell-surface and associated diffusion. Although C'Dots have a strong silica coating, osteocytes have been shown to have low pH capabilities used in localized bone mineral resorption (44, 45). They may be able to degrade the endocytosed C'Dots with their highly active ATPase proton pumps. However, it is currently unknown if the C'Dots are being actively degraded or ejected into circulation.

Beyond co-localization data, potential endocytosis and cycling of C'Dots was also suggested by the optimization experiment for incubation time. This experiment revealed interesting biphasic fluorescent intensity during subsequent timepoints. Unexpectedly, male and female mice were observed to have different trends, with females having stronger differ-

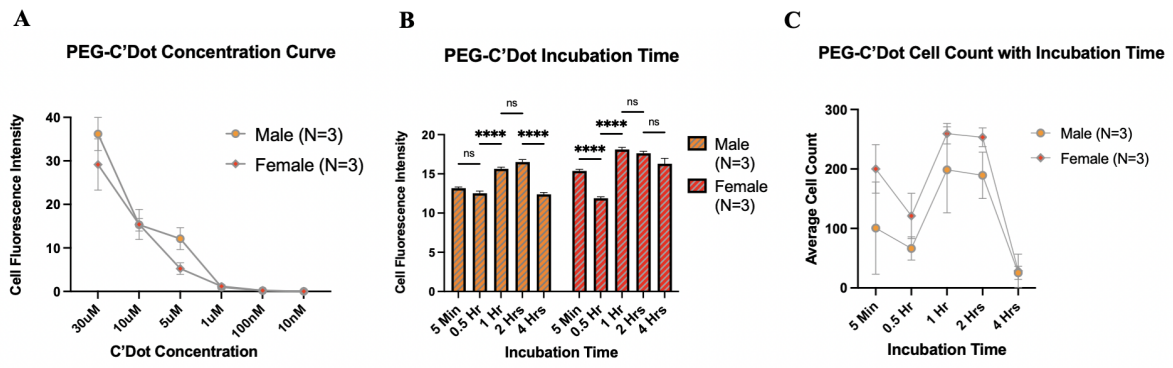

Fig. 4. Experimental validation and optimization of non-functionalized PEG-C'Dots as a novel osteocyte imaging probe. A) Concentration dose-response intensity signal for PEG-C'Dots was lost at 1µM. Optimal sub-saturation signal was selected at 10µM, which was significantly lower than signal at 30µM, but retains a signal strongly above baseline fluorescence. Data points represent the mean peak intensity for individual 'cell' ROIs. Significant differences were seen at distinct concentrations, but no significant differences were seen between groups with the same concentration. B) Incubation of PEG-C'Dots reveals distinct trends between male and female mice. 3D 'cell' objects were segmented in ImageJ from imaged z-stacks, and all quantified objects were used to find the mean intensity for each individual mouse. Signal was retained out to 4 hours of incubation. Significant increases and decreases in intensity were observed, and the trends are distinct between the sexes. C) Cell count for male and female mice at each timepoint. Counts were averaged across all mice in the same experimental group and timepoint. $^{*}p \leq 0.05$, error bars represent SEM, n=3 mice per group.

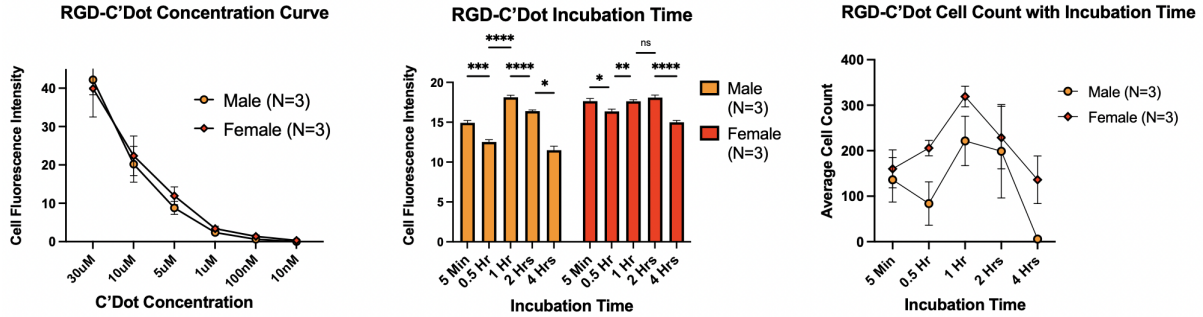

Fig. 5. Validation and optimization of functionalized RGD-C'Dots use as a osteocyte integrin targeted probe. A) Concentration dose-response intensity signal for RGD-C'Dots was lost at 100nM, a lower concentration than the control C'Dots. Optimal sub-saturation signal was again selected at 10µM. Data points represent the mean peak intensity for individual 'cell' ROIs. Significant differences were seen at distinct concentrations, but as with control C'Dots, no significant differences were seen between groups with the same concentration. B) RGD-C'Dot intensity based on incubation time was distinct from the dynamics observed in control C'Dots, and had a reversal in biphasic trend between the sexes. Signal was again lost after 4 hours. C) Cell count for male and female mice at each timepoint. Values were averaged across mice. $^{*}p \leq 0.05$, error bars represent SEM, n=3 mice per group.

ences in intensity during the first three timepoints. This trend was then seen in males when using the integrin targeting RGD-C'Dots. This change suggests that functionalization of the C'Dots and binding to integrins has somehow altered their metabolism and clearance within the LCS. The differences between control PEG-C'Dots and targeted RGD-C'Dots support potential cycling of RDG-C'Dot bound-integrins within osteocytes *in vivo*. Integrin cycling has been shown in other bone cells (20), but has not previously been reported in osteocytes. Based on their integral role in mechanobiology, understanding the dynamics of integrins *in vivo* will be a valuable tool in studying cellular accommodation, desensitization of osteocytes to mechanical loading, and osteocyte metabolism and intracellular trafficking.

Distinct trends in fluorescent signal were also observed between male and female mice in the clearance rate study. The sexual dimorphism of C'Dot metabolism and clearance was strongly seen, with females retaining signal for much longer compared to males. Female control PEG-C'Dots also exhibited the strongest intensity over time and male control PEG-C'Dots showed the lowest. Male control mice also lost signal 30 minutes prior to RDG-C'Dots mice. This may align with our original hypothesis that functionalization can allow for longer signal retention, however it is curious that it is only observed in male mice. That C'Dot clearance from the LCS appears to be sexually dimorphic was an unexpected finding. However, sex differences have been found in osteocyte protein expression (46) and sex hormones are known to have sizeable impacts on bone health and homeostasis (47, 48). Those sex dependent mechanisms may also have a role in the membrane dynamics of bone cells. Sex differences in endocytosis of membrane proteins such as integrins represents an interesting field of research for understanding sexual dimorphism in osteocyte function and could be a potential target for minimizing bone loss in ageing, especially for postmenopausal women. For example, bisphosphonates such as incadronate are potent anti-resorption drugs, and they are also known to inhibit endocytosis (49, 50).

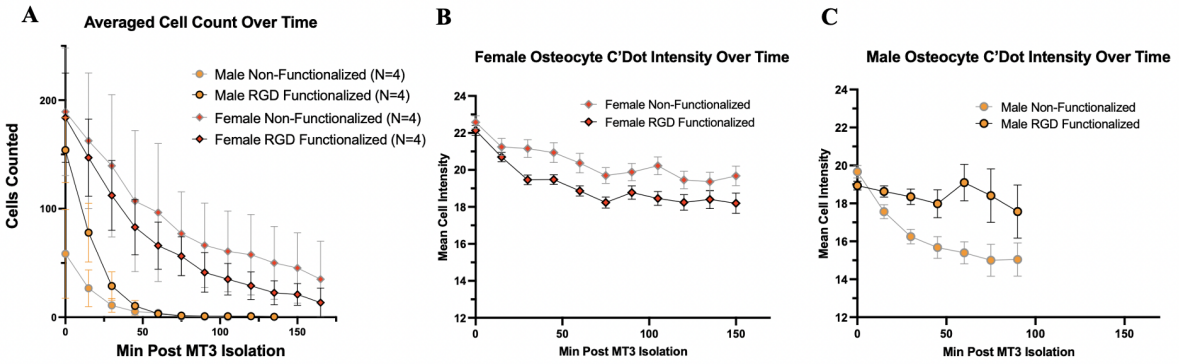

Fig. 6. Analysis of imaged non-functionalized PEG-C'Dot and functionalized RGD-C'Dot z-stacks over time reveals unique clearance between male and female mice. A) Number of 3D 'cells' were counted over time, out to almost 3 hours post MT3 isolation. Z-stacks were taken 15 minutes apart using an automated script in Thor software. 3D objects or 'cells' were quantified from each z-stack using an ImageJ macro. Male signal is negligible after one hour, while female signal remains out to the end of the experiment. Targeted RGD-C'Dots and Control PEG-C'Dots groups are not significantly different within each sex. N= 3 or 4 mice per group. B,C) Mean intensity for each counted cell was averaged within experimental group at each timepoint. Between 1 and 700 cells were averaged for each data point. Female RGD and Control were significantly different at one timepoint. ** $p \leq 0.01$. Error bars = SEM.

Overall, our results prove the use of ultrasmall and bright particle probes like C'Dots as potent *in vivo* osteocyte probes, likely able to reveal details of endocytosis and membrane dynamics in osteocytes, which to the best of our knowledge has not been previously observed *in vivo*. Additionally, sexual dimorphism in osteocyte metabolism and C'Dot clearance was observed, potentially providing a novel area of research to target for bone diseases. Future studies will confirm endocytosis of control PEG-C'Dots and their targeted analogue, i.e., RGD-C'Dots, localize their movement over short timeframes to track intravital integrin metabolism in osteocytes, and interrogate sex-specific differences in osteocyte dynamics.

ACKNOWLEDGEMENTS

We thank Karly Hooper for maintaining mouse colonies for use in these experiments, along with the entire CARE staff in Weill Hall. This work was supported by the Department of Biomedical Engineering at Cornell University.

Bibliography

1. Bonewald, L. F. The amazing osteocyte. Journal of Bone and Mineral Research 26, 229–238 (2011).
2. Choi, J. U. A., Kijas, A. W., Lauko, J. Rowan, A. E. The Mechanosensory Role of Osteocytes and Implications for Bone Health and Disease States. Frontiers in Cell and Developmental Biology 9, (2022).
3. Schaffler, M. B. Kennedy, O. D. Osteocyte Signaling in Bone. Curr Osteoporos Rep 10, 118–125 (2012).
4. Klein-Nulend, J., Bakker, A. D., Bacabac, R. G., Vatsa, A. Weinbaum, S. Mechanosensation and transduction in osteocytes. Bone 54, 182–190 (2013).
5. Lu, X. L., Huo, B., Chiang, V. Guo, X. E. Osteocytic network is more responsive in calcium signaling than osteoblastic network under fluid flow. Journal of Bone and Mineral Research 27, 563–574 (2012).
6. Weinkamer, R., Kollmannsberger, P. Fratzl, P. Towards a Connectomic Description of the Osteocyte Lacunocanalicular Network in Bone. Curr Osteoporos Rep 17, 186–194 (2019).
7. McNamara, L. m., Majeska, R. j., Weinbaum, S., Friedrich, V. Schaffler, M. b. Attachment of Osteocyte Cell Processes to the Bone Matrix. The Anatomical Record 292, 355–363 (2009).
8. Qin, L., Liu, W., Cao, H. Xiao, G. Molecular mechanosensors in osteocytes. Bone Res 8, 1–24 (2020).
9. Woo, S. M., Rosser, J., Dusevich, V., Kalajzic, I. Bonewald, L. F. Cell Line IDG-SW3 Replicates Osteoblast-to-Late-Osteocyte Differentiation in vitro and Accelerates Bone Formation in vivo. J Bone Miner Res 26, 2634–2646 (2011).
10. Wang, L., You, X., Zhang, L., Zhang, C. Zou, W. Mechanical regulation of bone remodeling. Bone Res 10, 16 (2022).
11. Geoghegan, I. P., Hoey, D. A. McNamara, L. M. Integrins in Osteocyte Biology and Mechanotransduction. Curr Osteoporos Rep 17, 195–206 (2019).
12. Haugh, M. G., Vaughan, T. J. McNamara, L. M. The role of integrin αVβ3 in osteocyte mechanotransduction. Journal of the Mechanical Behavior of Biomedical Materials 42, 67–75 (2015).
13. Thi, M. M., Suadicani, S. O., Schaffler, M. B., Weinbaum, S. Spray, D. C. Mechanosensory responses of osteocytes to physiological forces occur along processes and not cell body and require αVβ3 integrin. Proceedings of the National Academy of Sciences 110, 21012–21017 (2013).
14. Gu, Z., Noss, E. H., Hsu, V. W. Brenner, M. B. Integrins traffic rapidly via circular dorsal ruffles and macropinocytosis during stimulated cell migration. J Cell Biol 193, 61–70 (2011).
15. Moreno-Layseca, P., Icha, J., Hamidi, H. Ivaska, J. Integrin trafficking in cells and tissues. Nat Cell Biol 21, 122–132 (2019).
16. Rainero, E. Norman, J. C. Late endosomal and lysosomal trafficking during integrin-mediated cell migration and invasion. BioEssays 35, 523–532 (2013).
17. Roberts, M., Barry, S., Woods, A., van der Sluijs, P. Norman, J. PDGF-regulated rab4-dependent recycling of αvβ3 integrin from early endosomes is necessary for cell adhesion and spreading. Current Biology 11, 1392–1402 (2001).
18. White, D. P., Caswell, P. T. Norman, J. C. αvβ3 and α5β1 integrin recycling pathways dictate downstream Rho kinase signaling to regulate persistent cell migration. The Journal of Cell Biology 177, 515 (2007).
19. Woods, A. J., White, D. P., Caswell, P. T. Norman, J. C. PKD1/PKCμ promotes αvβ3 integrin recycling and delivery to nascent focal adhesions. EMBO J 23, 2531–2543 (2004).
20. Zhou, S., Zu, Y., Zhuang, F. Yang, C. Hypergravity-induced enrichment of β1 integrin on the cell membranes of osteoblast-like cells via caveolae-dependent endocytosis. Biochemical and Biophysical Research Communications 463, 928–933 (2015).
21. Wang, Y., McNamara, L. M., Schaffler, M. B. Weinbaum, S. A model for the role of integrins in flow induced mechanotransduction in osteocytes. Proceedings of the National Academy of Sciences 104, 15941–15946 (2007).
22. Batra, N., Kar, R. Jiang, J. X. Gap junctions and hemichannels in signal transmission, function and development of bone. Biochimica et Biophysica Acta (BBA) - Biomembranes 1818, 1909–1918 (2012).
23. Mizuno, H., Kikuta, J. Ishii, M. In vivo live imaging of bone cells. Histochem Cell Biol 149, 417–422 (2018).
24. Lewis, K. J. et al. Osteocyte calcium signals encode strain magnitude and loading frequency in vivo. Proceedings of the National Academy of Sciences 114, 11775–11780 (2017).
25. Maeda, H. et al. Real-time intravital imaging of pH variation associated with osteoclast activity. Nat Chem Biol 12, 579–585 (2016).
26. Minoshima, M. et al. In Vivo Multicolor Imaging with Fluorescent Probes Revealed the Dynamics and Function of Osteoclast Proton Pumps. ACS Cent. Sci. 5, 1059–1066 (2019).
27. Ma, K. et al. Control of Ultrasmall Sub-10 nm Ligand-Functionalized Fluorescent Core–Shell Silica Nanoparticle Growth in Water. Chem. Mater. 27, 4119–4133 (2015).
28. Erstling, J. A. et al. Ultrasmall, Bright, and Photostable Fluorescent Core–Shell Aluminosilicate Nanoparticles for Live-Cell Optical Super-Resolution Microscopy. Adv Mater 33, e2006829 (2021).
29. Choi, J. et al. Core-shell silica nanoparticles as fluorescent labels for nanomedicine. JBO 12, 064007 (2007).
30. Wang, L., Ciani, C., Doty, S. B. Fritton, S. P. Delineating bone's interstitial fluid pathway in vivo. Bone 34, 499–509 (2004).
31. Phillips, E. et al. Clinical translation of an ultrasmall inorganic optical-PET imaging nanoparticle probe. Sci Transl Med 6, 260ra149 (2014).
32. Zanoni, D. K. et al. Use of Ultrasmall Core-Shell Fluorescent Silica Nanoparticles for Image-Guided Sentinel Lymph Node Biopsy in Head and Neck Melanoma: A Nonrandomized Clinical Trial. JAMA Netw Open 4, e211936 (2021).
33. Herz, E., Ow, H., Bonner, D., Burns, A. Wiesner, U. Dye structure–optical property correlations in near-infrared fluorescent core-shell silica nanoparticles. Journal of Materials Chemistry 19, 6341–6347 (2009).
34. Larson, D. R. et al. Silica Nanoparticle Architecture Determines Radiative Properties of Encapsulated Fluorophores. Chem. Mater. 20, 2677–2684 (2008).
35. Kohle, F. F. E., Hinckley, J. A. Wiesner, U. B. Dye Encapsulation in Fluorescent Core–Shell Silica Nanoparticles as Probed by Fluorescence Correlation Spectroscopy. J. Phys. Chem. C 123, 9813–9823 (2019).
36. Barteau, K. P. et al. Quantitative Measure of the Size Dispersity in Ultrasmall Fluorescent Organic–Inorganic Hybrid Core–Shell Silica Nanoparticles by Small-Angle X-ray Scattering. Chem. Mater. 31, 643–657 (2019).

37. Ma, K., Zhang, D., Cong, Y. Wiesner, U. Elucidating the Mechanism of Silica Nanoparticle PEGylation Processes Using Fluorescence Correlation Spectroscopies. Chem. Mater. 28, 1537–1545 (2016).
38. Ma, K. Wiesner, U. Modular and Orthogonal Post-PEGylation Surface Modifications by Insertion Enabling Penta-Functional Ultrasmall Organic-Silica Hybrid Nanoparticles. Chem. Mater. 29, 6840–6855 (2017).
39. Chen, F. et al. Ultrasmall targeted nanoparticles with engineered antibody fragments for imaging detection of HER2-overexpressing breast cancer. Nat Commun 9, 4141 (2018).
40. Zhang, L. et al. Engineered Ultrasmall Nanoparticle Drug-Immune Conjugates with "Hit and Run" Tumor Delivery to Eradicate Gastric Cancer. Advanced Therapeutics n/a, 2200209.
41. Benezra, M. et al. Ultrasmall Integrin-Targeted Silica Nanoparticles Modulate Signaling Events and Cellular Processes in a Concentration-Dependent Manner. Small 11, 1721–1732 (2015).
42. Chen, F. et al. Cancer-Targeting Ultrasmall Silica Nanoparticles for Clinical Translation: Physicochemical Structure and Biological Property Correlations. Chem Mater 29, 8766–8779 (2017).
43. Benezra, M. et al. Multimodal silica nanoparticles are effective cancer-targeted probes in a model of human melanoma. J Clin Invest 121, 2768–2780 (2011).
44. Jähn, K. et al. Osteocytes Acidify Their Microenvironment in Response to PTHrP In Vitro and in Lactating Mice In Vivo. Journal of Bone and Mineral Research 32, 1761–1772 (2017).
45. Qing, H. et al. Demonstration of osteocytic perilacunar/canalicular remodeling in mice during lactation. Journal of Bone and Mineral Research 27, 1018–1029 (2012).
46. Youlten, S. E. et al. Osteocyte transcriptome mapping identifies a molecular landscape controlling skeletal homeostasis and susceptibility to skeletal disease. Nat Commun 12, 2444 (2021).
47. Chen, J.-F., Lin, P.-W., Tsai, Y.-R., Yang, Y.-C. Kang, H.-Y. Androgens and Androgen Receptor Actions on Bone Health and Disease: From Androgen Deficiency to Androgen Therapy. Cells 8, 1318 (2019).
48. Noirrit-Esclassan, E. et al. Critical Role of Estrogens on Bone Homeostasis in Both Male and Female: From Physiology to Medical Implications. Int J Mol Sci 22, 1568 (2021).
49. Teramura, K. et al. Incadronate inhibits osteoporosis in ovariectomized rats. Eur J Pharmacol 457, 51–56 (2002).
50. Iguchi, K., Matsunaga, S., Nakano, T., Usui, S. Hirano, K. Inhibition of caveolin-1 expression by incadronate in PC-3 prostate cells. Anticancer Res 26, 2977–2981 (2006).